

Submicrometer-wide amorphous and polycrystalline anatase TiO₂ waveguides for microphotonic devices

Jonathan D. B. Bradley, Christopher C. Evans, Jennifer T. Choy, Orad Reshef, Parag B. Deotare, François Parsy, Katherine C. Phillips, Marko Lončar, and Eric Mazur*

School of Engineering and Applied Sciences, Harvard University, 9 Oxford Street, Cambridge, Massachusetts 02138, USA

*mazur@seas.harvard.edu

Abstract: We demonstrate amorphous and polycrystalline anatase TiO₂ thin films and submicrometer-wide waveguides with promising optical properties for microphotonic devices. We deposit both amorphous and polycrystalline anatase TiO₂ using reactive sputtering and define waveguides using electron-beam lithography and reactive ion etching. For the amorphous TiO₂, we obtain propagation losses of 0.12 ± 0.02 dB/mm at 633 nm and 0.04 ± 0.01 dB/mm at 1550 nm in thin films and 2.6 ± 0.5 dB/mm at 633 nm and 0.4 ± 0.2 dB/mm at 1550 nm in waveguides. Using single-mode amorphous TiO₂ waveguides, we characterize microphotonic features including microbends and optical couplers. We show transmission of 780-nm light through microbends having radii down to 2 μm and variable signal splitting in microphotonic couplers with coupling lengths of 10 μm.

©2012 Optical Society of America

OCIS codes: (130.3120) Integrated optics devices; (130.3130) Integrated optics materials; (130.4310) Integrated optics, Nonlinear; (230.7370) Waveguides; (310.1860) Thin films, Deposition and fabrication; (310.6860) Thin films, optical properties.

References and links

1. P. R. Villeneuve, J. S. Foresi, J. Ferrera, E. R. Thoen, G. Steinmeyer, S. Fan, J. D. Joannopoulos, L. C. Kimerling, H. I. Smith, and E. P. Ippen, "Photonic-bandgap microcavities in optical waveguides," *Nature* **390**(6656), 143–145 (1997).
2. L. M. Tong, R. R. Gattass, J. B. Ashcom, S. L. He, J. Y. Lou, M. Y. Shen, I. Maxwell, and E. Mazur, "Subwavelength-diameter silica wires for low-loss optical wave guiding," *Nature* **426**(6968), 816–819 (2003).
3. V. R. Almeida, C. A. Barrios, R. R. Panepucci, and M. Lipson, "All-optical control of light on a silicon chip," *Nature* **431**(7012), 1081–1084 (2004).
4. M. T. Hill, H. J. S. Dorren, T. De Vries, X. J. Leijtens, J. H. Den Besten, B. Smalbrugge, Y.-S. Oei, H. Binsma, G.-D. Khoe, and M. K. Smit, "A fast low-power optical memory based on coupled micro-ring lasers," *Nature* **432**(7014), 206–209 (2004).
5. H. Park, A. W. Fang, R. Jones, O. Cohen, O. Raday, M. N. Sysak, M. J. Paniccia, and J. E. Bowers, "A hybrid AlGaInAs-silicon evanescent waveguide photodetector," *Opt. Express* **15**(10), 6044–6052 (2007).
6. C. Koos, P. Vorreau, T. Vallaitis, P. Dumon, W. Bogaerts, R. Baets, B. Esembeson, I. Biaggio, T. Michinobu, F. Diederich, W. Freude, and J. Leuthold, "All-optical high-speed signal processing with silicon-organic hybrid slot waveguides," *Nat. Photonics* **3**(4), 216–219 (2009).
7. X. Guo, M. Qiu, J. M. Bao, B. J. Wiley, Q. Yang, X. N. Zhang, Y. G. Ma, H. K. Yu, and L. M. Tong, "Direct coupling of plasmonic and photonic nanowires for hybrid nanophotonic components and circuits," *Nano Lett.* **9**(12), 4515–4519 (2009).
8. B. J. Eggleton, B. Luther-Davies, and K. Richardson, "Chalcogenide photonics," *Nat. Photonics* **5**, 141–148 (2011).
9. R. L. Espinola, J. I. Dadap, R. M. Osgood, Jr., S. J. McNab, and Y. A. Vlasov, "Raman amplification in ultrasmall silicon-on-insulator wire waveguides," *Opt. Express* **12**(16), 3713–3718 (2004).
10. R. R. Gattass, G. T. Svacha, L. M. Tong, and E. Mazur, "Supercontinuum generation in submicrometer diameter silica fibers," *Opt. Express* **14**(20), 9408–9414 (2006).
11. R. Dekker, A. Driessen, T. Wahlbrink, C. Moormann, J. Niehusmann, and M. Först, "Ultrafast Kerr-induced all-optical wavelength conversion in silicon waveguides using 1.55 μm femtosecond pulses," *Opt. Express* **14**(18), 8336–8346 (2006).

12. L. Tong, J. Lou, R. R. Gattass, S. He, X. Chen, L. Liu, and E. Mazur, "Assembly of silica nanowires on silica aerogels for microphotonic devices," *Nano Lett.* **5**(2), 259–262 (2005).
13. T. Tsuchizawa, K. Yamada, H. Fukuda, T. Watanabe, Jun-ichi Takahashi, M. Takahashi, T. Shoji, E. Tamechika, S. Itabashi, and H. Morita, "Microphotonic devices based on silicon microfabrication technology," *IEEE J. Sel. Top. Quantum Electron.* **11**(1), 232–240 (2005).
14. M. A. Foster, K. D. Moll, and A. L. Gaeta, "Optimal waveguide dimensions for nonlinear interactions," *Opt. Express* **12**(13), 2880–2887 (2004).
15. M. A. Foster, A. C. Turner, M. Lipson, and A. L. Gaeta, "Nonlinear optics in photonic nanowires," *Opt. Express* **16**(2), 1300–1320 (2008).
16. J. T. Choy, B. J. M. Hausmann, T. M. Babinec, I. Bulu, M. Khan, P. Maletinsky, A. Yacoby, and M. Lončar, "Enhanced single photon emission from a diamond-silver aperture," *Nat. Photonics* **5**(12), 738–743 (2011).
17. P. Koonath, D. R. Solli, and B. Jalali, "Limiting nature of continuum generation in silicon," *Appl. Phys. Lett.* **93**(9), 091114 (2008).
18. Q. Lin, J. Zhang, G. Piredda, R. W. Boyd, P. M. Fauchet, and G. P. Agrawal, "Dispersion of silicon nonlinearities in the near infrared region," *Appl. Phys. Lett.* **91**(2), 021111 (2007).
19. R. Mechiakh, F. Mèriche, R. Kremer, R. Bensaha, B. Boudine, and A. Boudrioua, "TiO₂ thin films prepared by sol-gel method for waveguiding applications: Correlation between the structural and optical properties," *Opt. Mater.* **30**(4), 645–651 (2007).
20. T. Alasaarela, T. Saastamoinen, J. Hiltunen, A. Säynätjoki, A. Tervonen, P. Stenberg, M. Kuittinen, and S. Honkanen, "Atomic layer deposited titanium dioxide and its application in resonant waveguide grating," *Appl. Opt.* **49**(22), 4321–4325 (2010).
21. J. D. B. Bradley, C. C. Evans, F. Parsy, K. C. Phillips, R. Senaratne, E. Marti, and E. Mazur, "Low-loss TiO₂ planar waveguides for nanophotonic applications," in *Proceedings of the 23rd Annual Meeting of the IEEE Photonics Society* (Institute of Electrical and Electronics Engineers, Denver, Colorado, 2010), pp. 313–314.
22. M. Furuhashi, M. Fujiwara, T. Ohshiro, M. Tsutsui, K. Matsubara, M. Taniguchi, S. Takeuchi, and T. Kawai, "Development of microfabricated TiO₂ channel waveguides," *AIP Advances* **1**, 032102/1–5 (2011).
23. K. Abe, E. Y. M. Teraoka, T. Kita, and H. Yamada, "Nonlinear optical waveguides with rutile TiO₂," *Proc. SPIE* **7940**, 79401G/1–7 (2011).
24. J. T. Choy, J. D. B. Bradley, P. B. Deotare, I. B. Burgess, C. C. Evans, E. Mazur, and M. Lončar, "Integrated TiO₂ resonators for visible photonics," *Opt. Lett.* **37**(4), 539–541 (2012).
25. Z.-F. Bi, L. Wang, X.-H. Liu, S.-M. Zhang, M.-M. Dong, Q.-Z. Zhao, X.-L. Wu, and K.-M. Wang, "Optical waveguides in TiO₂ formed by He ion implantation," *Opt. Express* **20**(6), 6712–6719 (2012).
26. J. M. Bennett, E. Pelletier, G. Albrand, J. P. Borgogno, B. Lazarides, C. K. Carniglia, R. A. Schmall, T. H. Allen, T. Tuttle-Hart, K. H. Guenther, and A. Saxer, "Comparison of the properties of titanium dioxide films prepared by various techniques," *Appl. Opt.* **28**(16), 3303–3317 (1989).
27. N. Sherwood-Droz and M. Lipson, "Scalable 3D dense integration of photonics on bulk silicon," *Opt. Express* **19**(18), 17758–17765 (2011).
28. R. Adair, L. L. Chase, and S. A. Payne, "Nonlinear refractive index of optical crystals," *Phys. Rev. B Condens. Matter* **39**(5), 3337–3350 (1989).
29. H. Long, A. P. Chen, G. Yang, Y. H. Li, and P. X. Lu, "Third-order optical nonlinearities in anatase and rutile TiO₂ thin films," *Thin Solid Films* **517**(19), 5601–5604 (2009).
30. C. C. Evans, J. D. B. Bradley, E. A. Martí-Panameño, and E. Mazur, "Mixed two- and three-photon absorption in bulk rutile (TiO₂) around 800 nm," *Opt. Express* **20**(3), 3118–3128 (2012).
31. K. Ikeda, R. E. Saperstein, N. Alic, and Y. Fainman, "Thermal and Kerr nonlinear properties of plasma-deposited silicon nitride/ silicon dioxide waveguides," *Opt. Express* **16**(17), 12987–12994 (2008).
32. S. P. S. Porto, P. A. Fleury, and T. C. Damen, "Raman spectra of TiO₂, MgF₂, ZnF₂, FeF₂, and MnF₂," *Phys. Rev.* **154**(2), 522–526 (1967).
33. T. Ohsaka, F. Izumi, and Y. Fujiki, "Raman spectrum of anatase, TiO₂," *J. Raman Spectrosc.* **7**(6), 321–324 (1978).
34. P. K. Tien, "Light waves in thin films and integrated Optics," *Appl. Opt.* **10**(11), 2395–2413 (1971).
35. N. Daldosso, M. Melchiorri, F. Riboli, F. Sbrana, L. Pavesi, G. Pucker, C. Kompocholis, M. Crivellari, P. Bellutti, and A. Lui, "Fabrication and optical characterization of thin two-dimensional Si₃N₄ waveguides," *Mater. Sci. Semicond. Process.* **7**(4-6), 453–458 (2004).
36. N. Martin, C. Rousselot, D. Rondot, F. Palmino, and R. Mercier, "Microstructure modification of amorphous titanium dioxide thin films during annealing treatment," *Thin Solid Films* **300**(1-2), 113–121 (1997).
37. Y. Vlasov and S. J. McNab, "Losses in single-mode silicon-on-insulator strip waveguides and bends," *Opt. Express* **12**(8), 1622–1631 (2004).
38. J. S. Foresi, M. R. Black, A. M. Agarwal, and L. C. Kimerling, "Losses in polycrystalline silicon waveguides," *Appl. Phys. Lett.* **68**(15), 2052–2054 (1996).
39. T. Barwicz and H. I. Smith, "Evolution of line-edge roughness during fabrication of high-index-contrast microphotonic devices," *J. Vac. Sci. Technol. B* **21**(6), 2892–2896 (2003).
40. M. Gnan, D. S. Macintyre, M. Sorel, R. M. De La Rue, and S. Thoms, "Enhanced stitching for the fabrication of photonic structures by electron beam lithography," *J. Vac. Sci. Technol. B* **25**(6), 2034–2037 (2007).

41. S. Lardenois, D. Pascal, L. Vivien, E. Cassan, S. Laval, R. Orobtcouk, M. Heitzmann, N. Bouzaida, and L. Mollard, "Low-loss submicrometer silicon-on-insulator rib waveguides and corner mirrors," *Opt. Lett.* **28**(13), 1150–1152 (2003).
 42. J. Cardenas, C. B. Poitras, J. T. Robinson, K. Preston, L. Chen, and M. Lipson, "Low loss etchless silicon photonic waveguides," *Opt. Express* **17**(6), 4752–4757 (2009).
 43. R. J. Bojko, J. Li, L. He, T. Baehr-Jones, M. Hochberg, and Y. Aida, "Electron beam lithography writing strategies for low loss, high confinement silicon optical waveguides," *J. Vac. Sci. Technol.* **29**(6), 06F309 (2011).
-

1. Introduction

The development of nanoscale optical waveguides with low losses has led to miniature, efficient photonic devices for applications in the fields of communications, computing, metrology, and sensing [1–8]. Nanoscale waveguides strongly confine light by utilizing high-refractive-index-contrast materials, resulting in high optical intensities for efficient nonlinear light-matter interactions [9–11], small bending radii, and microscale device footprints [12, 13]. Furthermore, controlling nanoscale features enables one to engineer critical waveguide properties, such as the number of supported modes, the strength of signal coupling between adjacent waveguides, effective nonlinearity, and waveguide dispersion [14, 15].

Standard nanoscale waveguide materials, such as silica and silicon, have limitations despite their low cost and compatibility with current photonic and electronic platforms. Fiber-based silica nanowires have limited scalability due to labor-intensive assembly [12]. Meanwhile silicon, a scalable material with mature fabrication processes, offers transparency only at wavelengths above 1.1 μm . Limited transparency inhibits its use in emerging applications such as quantum photonics, where promising single-photon sources emit at visible wavelengths [16]. Silicon also exhibits strong two-photon absorption at telecommunications wavelengths, which leads to free-carrier absorption and prohibits many nonlinear devices [11, 17, 18]. Therefore, we require complimentary nanoscale waveguide materials to meet the demands of future visible and near infrared linear and nonlinear microphotonic systems.

Recently titanium dioxide (TiO_2) has attracted attention as a prospective photonic material [19–25]. Amorphous and polycrystalline TiO_2 thin films can be deposited at low temperatures (< 650 K) using conventional, scalable methods [26], allowing for straightforward integration with other on-chip devices [27]. TiO_2 has a high refractive index ($n \approx 2.4$), which allows for high-refractive-index-contrast waveguides and strong light confinement. Due to its large bandgap ($E_g = 3.1$ eV), TiO_2 is transparent over a broad wavelength range that includes the visible and near-infrared. In addition, TiO_2 is a promising nonlinear photonic material, having a high nonlinearity (≥ 25 times higher than silica) [28–30] and low two-photon absorption for wavelengths above 800 nm [30]. This combination of properties puts TiO_2 into a similar class as silicon nitride; however, TiO_2 exhibits both a higher linear refractive index (2.4 for TiO_2 versus 2.0 for silicon nitride at 800 nm) and nonlinear refractive index (9×10^{-19} m^2/W for bulk rutile TiO_2 versus 2.4×10^{-19} m^2/W for silicon nitride) [28, 31].

Amorphous TiO_2 waveguides on oxidized silicon [22, 24] and waveguides formed in single-crystal rutile [23, 25] have been demonstrated. The reported amorphous waveguide structures were limited to large dimensions (> 1 μm) [22] or only investigated for visible-wavelength operation [24]. For practical on-chip devices, such waveguides must have submicrometer dimensions to support single-mode operation. Small dimensions are also necessary for flexibility in the design of basic features such as waveguide bends and optical-couplers on the microscale. In addition, anatase microphotonic waveguides have not been developed, despite having a higher reported nonlinearity [29] and requiring lower fabrication temperatures than crystalline rutile waveguides.

In this paper, we report on TiO_2 strip waveguides with submicrometer dimensions and promising optical properties for on-chip photonic devices. We fabricate both amorphous and polycrystalline anatase TiO_2 thin films and compare their structural and optical properties. We

then fabricate strip waveguides and measure their propagation losses at visible and near-infrared wavelengths. Finally, we investigate microphotonic features to assess the prospective application of TiO₂ waveguides in photonic devices.

2. TiO₂ thin films

2.1 Thin-film deposition

We deposit TiO₂ thin films on oxidized silicon substrates (3- μm -thick SiO₂) using reactive radio frequency (RF) magnetron sputtering. We prepare 0.25- μm -thick TiO₂ films under the conditions summarized in Table 1. Films deposited at a substrate temperature of 290 K and 625 K yield amorphous and anatase TiO₂ thin-films, respectively [26]. We select optimal O₂ flow rates and RF powers to obtain stoichiometric, highly transparent TiO₂ thin films [21].

Table 1. Reactive RF Sputtering Parameters

Deposition Parameter	Amorphous TiO ₂	Anatase TiO ₂
Temperature (K)	290	625
Pressure (mTorr)	2	2
Ar flow (sccm)	40	40
O ₂ flow (sccm)	4.4	20
RF power (W)	158	200
Time (min.)	300	1390

2.2 Thin-film characterization

We determine the crystalline structure of the TiO₂ thin films using Raman spectroscopy. To avoid background signal from the silicon substrate, we measure Raman spectra of thin films deposited on a glass substrates using identical deposition parameters, as shown in Fig. 1 (we observe similar spectra for the films deposited on oxidized silicon substrates, with additional silicon peaks at 300 and 519 cm⁻¹). For films deposited at 290 K, we observe no Raman peaks (Fig. 1, top) which indicates that the TiO₂ phase is predominantly amorphous. Meanwhile, films deposited at 625 K display a strong peak at 144 cm⁻¹, and additional peaks at 194, 399, 514 and 639 cm⁻¹ (Fig. 1, bottom). We do not observe any of the peaks near 447, 612, or 826 cm⁻¹ associated with the Raman spectrum of rutile (which also includes a relatively weak peak around 143 cm⁻¹) [32]. The observed Raman peaks closely match those measured at 144, 197, 399, 516, and 639 cm⁻¹ in anatase single crystals [33], indicating that the TiO₂ phase is primarily anatase.

In order to compare the surface morphology of the thin films, we use scanning electron microscopy (SEM) and atomic force microscopy (AFM). Scanning electron micrographs of the surface of the films (Figs. 2(a) and 2(b)) show that the amorphous structure is granular, while the anatase film consists of densely packed nanocrystals. AFM scanning images, obtained in non-contact alternating current mode with a 9-nm-radius cantilever tip, reveal root mean square (RMS) roughness of 0.4 and 2.7 nm for the amorphous and anatase films, respectively (Figs. 2(c) and 2(d)).

We measure the optical properties of both TiO₂ films in the visible and near-infrared spectrum using a variable angle prism coupling system [34]. Table 2 summarizes the refractive indices of the TiO₂ films at 633, 826, 1310 and 1550 nm measured using transverse-electric (TE) polarized light. Both films have refractive indices of around 2.4 at 826 nm, with the anatase film having a slightly higher refractive index. Measurements using transverse-magnetic (TM) polarized light at 826 nm reveal a slight birefringence for both films, the TM indices being 0.006 and 0.012 higher in the amorphous and anatase films, respectively.

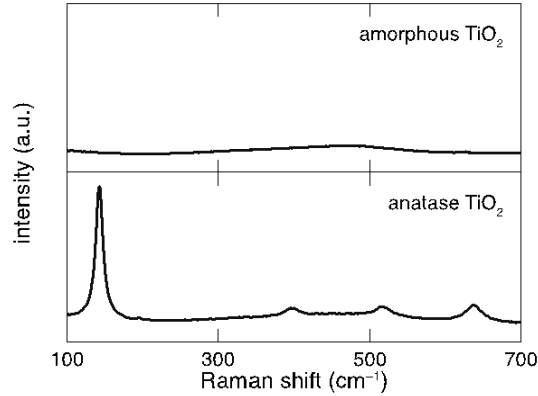


Fig. 1. Raman spectra of TiO₂ thin-films deposited by reactive RF magnetron sputtering at 290 K (top) and 625 K (bottom). The film deposited at 290 K has no measurable Raman peaks, indicating an amorphous structure, while the film deposited at 625 K shows peaks at 144, 194, 399, 514, and 639 cm⁻¹, which correspond to the anatase crystalline phase of TiO₂.

Table 2 also shows the thin-film propagation losses measured by scanning a fiber along the coupled planar waveguide mode normal to the surface of the film. Using a germanium detector, we collect scattered light versus position and fit the data to an exponential curve. The anatase films exhibit losses ranging from > 2.0 dB/mm at 633 nm (beyond the measurable limit of the prism coupling system) to 0.42 ± 0.08 dB/mm at 1550 nm. The amorphous TiO₂ thin-film propagation losses are significantly lower and are less wavelength-dependent, varying from 0.12 ± 0.02 dB/mm at 633 nm to 0.04 ± 0.01 dB/mm at 1550 nm.

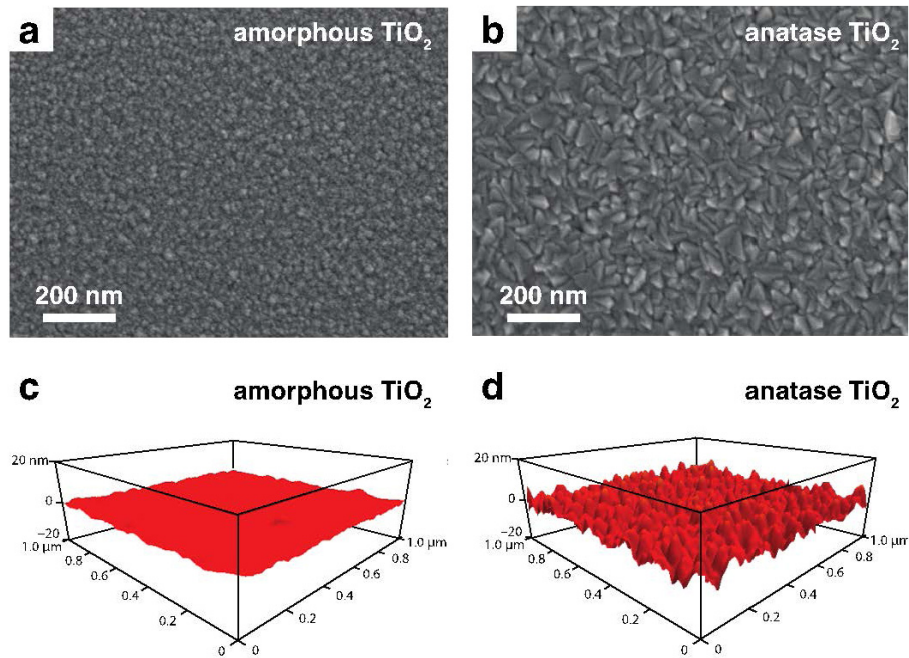


Fig. 2. Surface morphology of TiO₂ thin films: SEM images of (a) amorphous and (b) polycrystalline anatase thin-film surfaces; and AFM surface scans of (c) amorphous and (d) polycrystalline anatase thin-films showing RMS roughness of 0.4 and 2.7 nm, respectively.

Table 2. Refractive Indices and Propagation Losses of TiO₂ Thin Films*

Wavelength (nm)	Amorphous TiO ₂		Anatase TiO ₂	
	Refractive Index	Propagation Loss (dB/mm)	Refractive Index	Propagation Loss (dB/mm)
633	2.426	0.12	2.486	> 2.0
826	2.372	0.06	2.427	2.0
1310	2.323	0.04	2.375	0.91
1550	2.315	0.04	2.366	0.42

*The films are 0.25 μm thick, consisting of amorphous and polycrystalline anatase TiO₂ on oxidized silicon substrates. Both indices and losses are determined by prism coupling using TE-polarization. We estimate an uncertainty of ± 0.002 for the refractive index measurements and $\pm 20\%$ for the loss measurements.

3. Submicrometer-wide TiO₂ waveguides

3.1 Waveguide fabrication

We apply standard top-down fabrication methods to define submicrometer-wide waveguides in our amorphous and anatase TiO₂ thin films. First, we expose the waveguide pattern into a 300-nm-thick positive electron-beam (e-beam) resist layer (ZEP) on top of the TiO₂ film using a 100-keV electron-beam lithography system. The applied e-beam parameters include a $300 \times 300 \mu\text{m}^2$ write window, a beam current of 100 pA, and a dose of 400 $\mu\text{C}/\text{cm}^2$. After developing the exposed resist, we deposit a 50-nm-thick chromium film by e-beam evaporation and perform metal lift-off to form a metal etch mask. We then transfer the metal pattern into the TiO₂ film using electron cyclotron resonance reactive ion etching. The etch parameters include a CF₄ and H₂ gas mixture in a ratio of 4:1, a microwave power of 300 W, a substrate power of 150 W, and a chamber pressure of 5 mTorr. Using surface profilometry, we find that the etch rates of the amorphous and anatase films are approximately 50 and 60 nm/min, respectively. After etching, we remove the remaining metal mask using Cr-etchant, and apply a 1.6- μm -thick fluoropolymer top-cladding layer ($n = 1.39$). Finally, we cleave the chips to prepare waveguide end-facets.

Figures 3(a) and 3(b) show scanning electron micrographs of the resulting amorphous and anatase TiO₂ waveguides (without top-cladding), respectively. Both types of waveguides have relatively smooth, uniform sidewalls with slopes of approximately 75°. The cross-section of the anatase TiO₂ waveguide facet reveals the TiO₂ core to consist of close-packed vertical nanocrystalline columns (Fig. 2(b)).

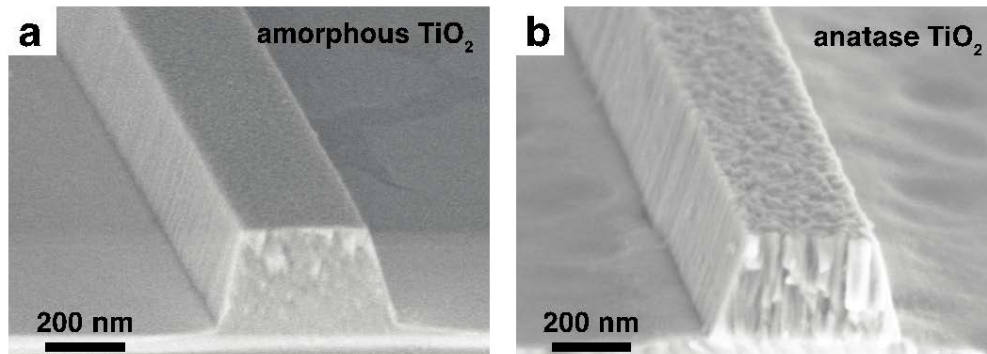


Fig. 3. SEM images of 0.3- μm -wide (a) amorphous and (b) polycrystalline anatase TiO₂ waveguides fabricated on oxidized silicon wafers using e-beam lithography and reactive ion etching.

3.2 Waveguide characterization

We investigate light transmission in 5-mm-long S-shaped waveguides with widths of 0.2, 0.3, 0.4, and 0.5 μm . The selected waveguide dimensions support guided modes in the wavelength

range 633–1550 nm. We chose a minimum bend radius of 60 μm to avoid significant bend-induced losses. Using a commercial finite-difference eigenmode solver, we determine that all waveguides are multimode at 633 nm, single-mode at 780 nm for widths of $\leq 0.3 \mu\text{m}$ (amorphous) and $0.2 \mu\text{m}$ (anatase), and single-mode at 1550 nm for widths of $\geq 0.4 \mu\text{m}$. Widths below $0.4 \mu\text{m}$ do not support a guided mode at 1550 nm.

We measure the optical propagation losses of the TiO_2 strip waveguides at 633, 780 and 1550 nm using the top-view camera method [35]. Light from a 633-nm HeNe, 780-nm diode, or a 1550-nm diode laser source is aligned and focused onto the input facets of the waveguides using an objective lens (633 and 780 nm) or lensed fiber (1550 nm) mounted on a piezoelectric-motor-controlled XYZ stage. We adjust the polarization of the incident light using a half-wave plate and a polarizer prior to the objective lens (633 and 780 nm) and a paddle-based polarization controller before the lensed fiber (1550 nm). We capture images using microscope-mounted CMOS (633 and 780 nm) and InGaAs (1550 nm) cameras and determine the transmission through the TiO_2 waveguides by analyzing the relative intensity of scattered light along the waveguides in the resulting images.

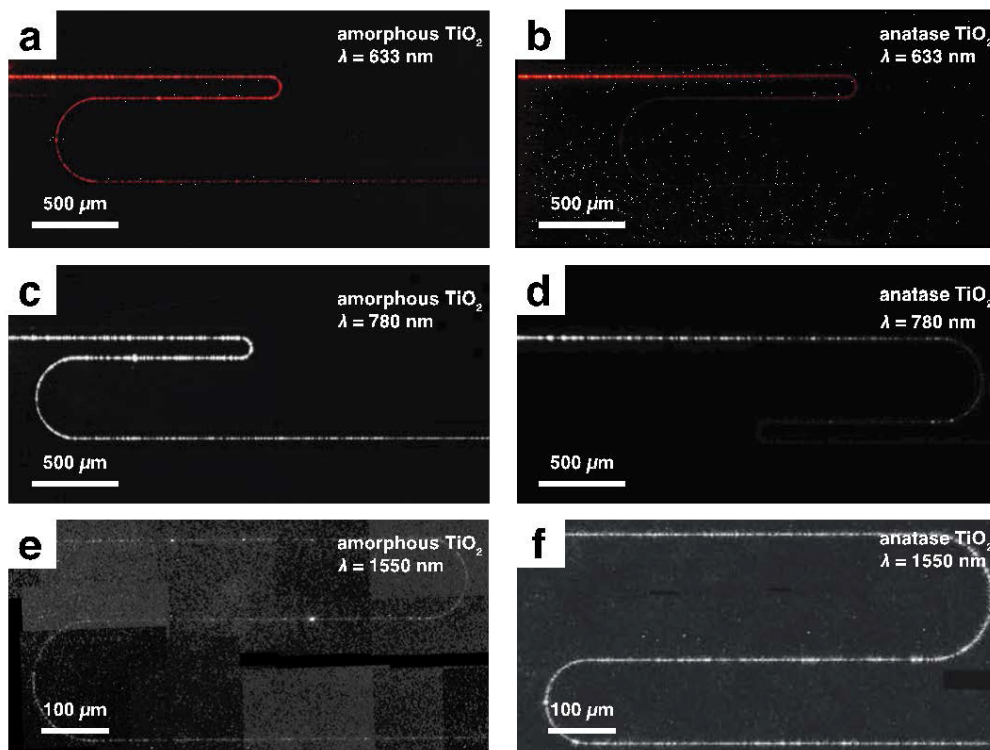


Fig. 4. Top-view CMOS (633 nm and 780 nm) and InGaAs (1550 nm) camera images showing light propagation at different wavelengths λ in amorphous and polycrystalline anatase TiO_2 waveguides. The waveguides are $0.2\text{-}\mu\text{m}$ wide (a–d) and $0.5\text{-}\mu\text{m}$ wide (e and f).

In Fig. 4 we show representative top-view camera images of visible and infrared light propagation in our amorphous (Figs. 4(a), 4(c) and 4(e)) and polycrystalline anatase (Figs. 4(b), 4(d) and 4(f)) waveguides. The propagation loss data corresponding to the representative images is shown in Figs. 5(a) and 5(b). Table 3 summarizes the propagation-loss data measured for different waveguide widths. The amorphous losses are considerably lower than the anatase losses at 633 and 780 nm. The uncertainty in the fit for the InGaAs camera measurements is rather high ($\pm 50\%$) due to the large relative background intensities in the

images. Therefore, we measure similar losses at 1550 nm in both types of TiO₂ waveguide within the experimental uncertainty.

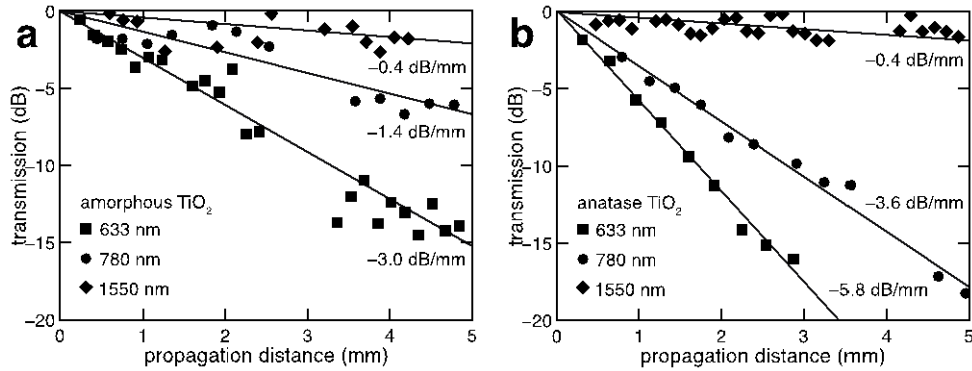


Fig. 5. Propagation losses in (a) amorphous and (b) polycrystalline anatase TiO₂ strip waveguides measured using the top-view camera method. The input light is TE-polarized and the waveguide widths are 0.2 μm (633 and 780 nm) and 0.5 μm (1550 nm).

Table 3. Propagation Losses in Amorphous and Anatase TiO₂ Waveguides*

Wavelength (nm)	Waveguide Width (μm)	Propagation Loss (dB/mm)	
		Amorphous TiO ₂	Anatase TiO ₂
633	0.2	3.0	5.8
	0.3	2.9	4.8
	0.4	2.6	6.1
	0.5	3.2	4.8
780	0.2	1.4	3.5
	0.3	2.2	3.5
	0.4	1.4	3.1
	0.5	0.9	3.8
1550	0.4	0.5	0.3
	0.5	0.4	0.4

*Measurement performed using the top-view camera method (TE-polarization). The uncertainty is $\pm 20\%$, $\pm 20\%$, and $\pm 50\%$ for the 633-, 780-, and 1550-nm measurements, respectively.

4. TiO₂ microphotonic features

4.1 Design and fabrication of microphotonic features

As a proof of principle, we investigate microphotonic features at 780 nm, near TiO₂'s half-bandgap and where nonlinear optical devices are feasible in bulk rutile TiO₂ [30]. We base our devices on a 0.3- μm -wide amorphous TiO₂ waveguide, which supports a single, well-confined TE-mode and has lower losses than similar anatase waveguides around 800 nm. To investigate waveguide bending losses, we fabricate waveguides with multiple bends having radii of 1–20 μm . In addition, we fabricate optical couplers consisting of two waveguides with adiabatic sine-bends into and out of a parallel coupling region. The spacing of the coupling region is 0.2 μm and its length, L , varies from 0 to 4 μm . We measure the transmission characteristics of the bends and optical couplers using the top-view camera method.

4.2 Micro-bends

Figure 6 summarizes the measurements and characterization of the TiO₂ microbends. Figure 6(a) shows the simulated electric field profile of the fundamental 780-nm TE mode confined

by the amorphous-TiO₂ waveguide. In Fig. 6(b), we display a top-view SEM image of a representative TiO₂ waveguide with microbends having radii r of 5 μm prior to cladding layer deposition. In Fig. 6(c), we show camera images of light transmission through cladded microbend features with $r = 20 \mu\text{m}$ (top), 10 μm (middle) and 5 μm (bottom). Figure 6(d) displays the measured transmission for varying r . The plot shows a minimal change in transmission as r is decreased to a value of 3 μm . At $r = 2 \mu\text{m}$ we observe a change in transmission of -9 dB that corresponds to an added loss of $< 1 \text{ dB}/90^\circ$ bend. For $r = 1 \mu\text{m}$, the transmission is below the measurable limit (-40 dB).

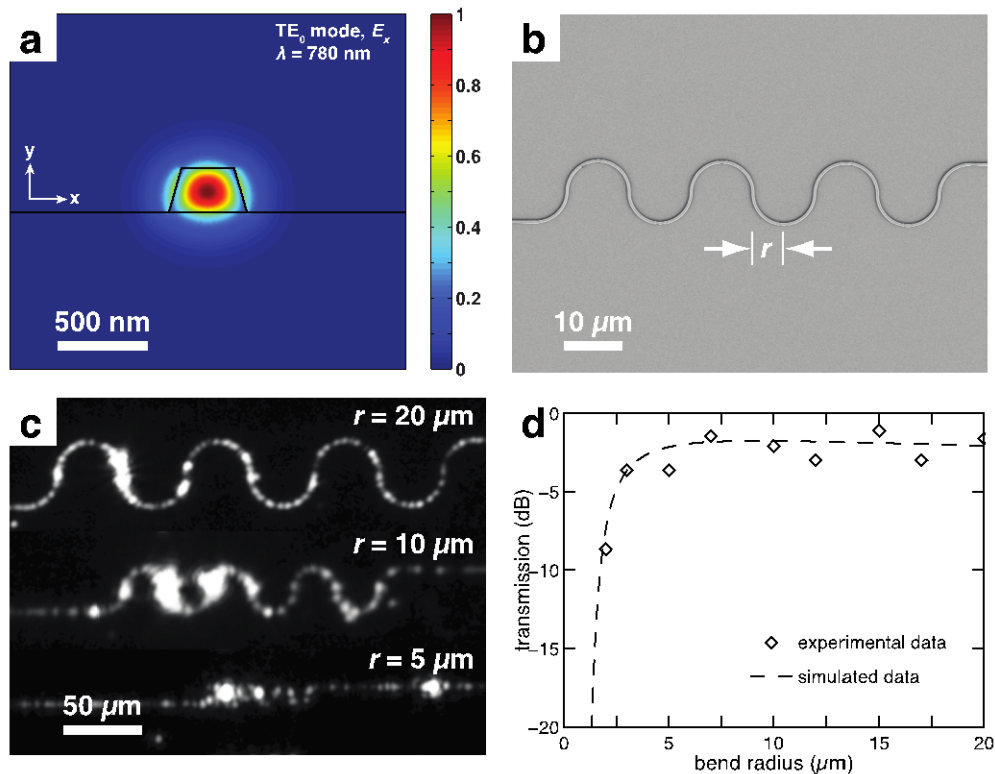


Fig. 6. (a) Calculated TE-like field profile of the fundamental 780-nm mode in a straight $0.25 \mu\text{m} \times 0.3 \mu\text{m}$ amorphous TiO₂ waveguide; (b) SEM top-view image of a bend-transmission test-feature consisting of a $0.25 \mu\text{m} \times 0.3 \mu\text{m}$ amorphous TiO₂ waveguide with fourteen consecutive 90° -bends with a radius r of 5 μm ; (c) CMOS camera images showing light transmission through test features with $r = 20 \mu\text{m}$ (top), $r = 10 \mu\text{m}$ (middle), and $r = 5 \mu\text{m}$ (bottom); (d) measured and simulated transmission for varying bend radii.

4.3 Optical-couplers

Figure 7(a) displays an SEM image of an optical-coupler (prior to cladding deposition) with a parallel interaction length $L = 4 \mu\text{m}$. Figure 7(b) shows optical images of light transmission in couplers with $L = 0 \mu\text{m}$ (top), $L = 2 \mu\text{m}$ (middle) and $L = 4 \mu\text{m}$ (bottom). By measuring the scattered intensity in each output branch of the coupler (I_{upper} and I_{lower}) we determine splitting ratios $I_{upper}/(I_{upper} + I_{lower})$ of 0.3, 0.6, and 0.9, respectively.

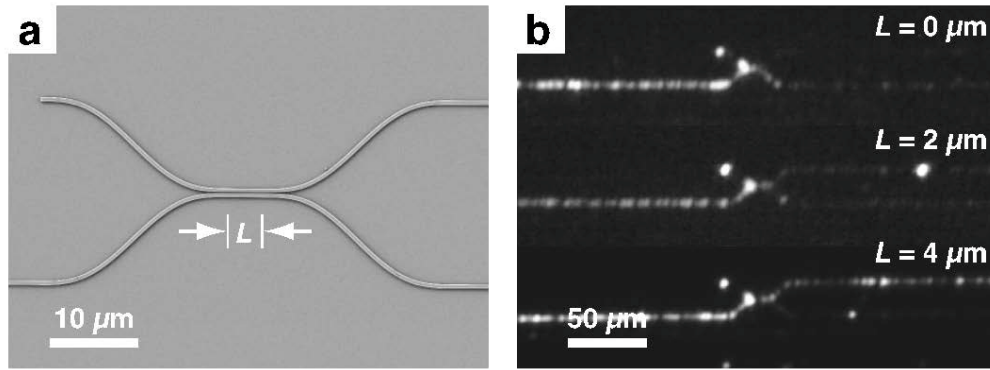


Fig. 7. TiO₂ microphotonic couplers: (a) SEM image of a TiO₂ optical-coupler with adiabatic input/output transitions and a parallel interaction region with a waveguide spacing of 0.2 μm and length, L , of 4 μm; (b) CMOS images showing splitting ratios (light transferred to the upper waveguide divided by the total transmitted intensity) of 0.3 (top), 0.6 (middle), and 0.9 (bottom) for $L = 0, 2$ and 4 μm, respectively (780-nm light, TE polarization).

5. Discussion

We show that by adjusting substrate temperature, oxygen flow rate and RF sputtering power, we can deposit waveguide-quality amorphous and polycrystalline-anatase TiO₂ thin films. At visible and near-infrared wavelengths, our amorphous TiO₂ thin films exhibit significantly lower propagation losses. The difference in propagation loss is most evident in the visible. In the 0.25-μm-thick films prepared for this study, we observe a pronounced visible streak of light across tens of mm in the amorphous film, but observe no measurable 633-nm-light propagation in the polycrystalline film. We partially attribute the difference in loss to the larger surface roughness in the anatase thin film. Despite having higher thin-film losses, the anatase phase of TiO₂ offers potential advantages for microphotonic devices in terms of greater thermal stability [36], higher refractive index, and higher nonlinearity [29]. Reduced nanocrystal size and smoother surfaces may lead to lower losses in the polycrystalline films.

We also demonstrate a suitable method for fabricating submicrometer-wide strip waveguides using both types of TiO₂ thin film. The amorphous TiO₂ strip waveguides have lower propagation losses at 633 and 780 nm than the anatase waveguides. As with the thin films, the difference is most significant at 633 nm, where we have recently demonstrated amorphous TiO₂ microring resonators for visible-light systems [24]. In both amorphous and polycrystalline waveguides, we measure losses on the order of 0.3–0.5 dB/mm at 1550 nm, which are comparable to those initially reported in other high-refractive-index-contrast photonic waveguides [2, 37, 38]. The comparable losses at 1550 nm can be explained by the reduced influence of surface and edge roughness, and the low optical confinement within the TiO₂ core (< 40%) whereby the majority of light propagates in the low-loss cladding layers.

The measured strip-waveguide propagation losses are sufficiently low for microphotonic devices requiring μm and mm waveguide lengths. However, we observe significantly higher propagation losses in our TiO₂ strip waveguides compared to the unstructured planar films, as is typical in high-refractive-index-contrast waveguides [39]. Moreover, the waveguide losses exhibit greater wavelength dependence than the thin film losses based on the relative values measured at 633 and 1550 nm. Several mechanisms may introduce additional losses in our strip waveguides, including radiation of higher-order modes, scattering due to core-cladding interfacial roughness, and e-beam write-field stitching errors [39, 40]. Each loss mechanism theoretically scales inversely with wavelength, consistent with observation. We may reduce waveguide losses towards the thin-film values using alternative waveguide geometries [41], complimentary fabrication methods [42], or specialized e-beam writing strategies [43].

By investigating amorphous TiO₂ microphotonic features, we show that light is transmitted through waveguide bends with radii down to 2 μm and demonstrate TiO₂ optical couplers. To gain insight into the loss mechanisms of the investigated bend structures, we compare the simulated transmission properties of TiO₂ microphotonic bends with our experimental results. In Fig. 6(d) we show the calculated transmission through micro-bends as a function of bend radius. The total calculated loss includes the losses due to modal overlap mismatch at the interface between straight and bent waveguides and between 90°-bends of opposite direction, radiation losses from the 90°-bends, and the experimental propagation loss of 2.2 ± 0.4 dB/mm measured in 300-nm-wide amorphous TiO₂ waveguides. We observe a good agreement between the calculated and experimental data. In the calculated data, the primary contribution to the total loss is the modal overlap mismatch at the interfaces, and not radiative loss due to the bend itself. For example, we calculate a bend-bend transition loss of 0.75 dB compared with a radiation loss of 0.01 dB for a 90° bend with $r = 2$ μm. For micro-bends with $r \leq 2$ μm, the transmission can be improved by incorporating adiabatic transitions. We also expect that comparably small bend radii are feasible in anatase waveguides due to their similar dimensions and refractive indices. These results, combined with the high optical confinement in TiO₂ waveguides, demonstrate that TiO₂ devices can be densely integrated on photonic chips.

To compare our optical-coupler measurements to the theoretical splitting ratios, we calculate the coupling distance by solving for the even and odd TE-polarized modes in the investigated structures. We calculate effective indices of 1.919 and 1.885, respectively, for which coupled-mode theory predicts a 100% coupling length of 12 μm. This value is consistent with the experimentally observed coupling ratios and lengths when we account for the additional effective coupling length introduced by the adiabatic input and output regions (6 μm). We measure a splitting-ratio of approximately 90% for an effective length of 10 μm. Our data shows that we can achieve strong coupling over short lengths, allowing for small footprints for devices such as ring resonators.

6. Conclusion

In conclusion, we have fabricated amorphous and polycrystalline anatase TiO₂ thin films and strip waveguides with submicrometer widths. We observe light propagation over mm-length scales at 633 and 780 nm, and measure losses of 0.4 ± 0.2 dB/mm in amorphous and anatase strip-waveguides at 1550 nm. The consistency between simulated and experimental micro-bend and optical-coupler results suggest that realizing complex micro-scale TiO₂ photonic devices can be achieved using the techniques reported here. These results demonstrate TiO₂ to be a novel and promising platform for visible to infrared microphotonic devices.

Acknowledgments

Several people contributed to the work described in this paper. All authors provided contributions to the basic ideas described in this work. JDBB, CCE., JTC, OR, PBD, FP, and KCP designed and carried out the experiments, and analyzed the results. ML and EM supervised the research and the development of the manuscript. JDBB. wrote the first draft of the manuscript; all authors subsequently took part in the revision process and approved the final copy of the manuscript. Rafael Gattass and Ruwan Senaratne contributed to the preliminary research and Laura Tucker and Phillip Munoz provided feedback on the manuscript throughout its development. The devices were fabricated at the Center for Nanoscale Systems at Harvard University. The research described in this paper was supported by the National Science Foundation under contract ECCS-0901469, the Harvard Quantum Optics Center, and the Fonds de recherche du Québec – Nature et technologies. JTC and PBD were partially supported by the Center for Excitonics, an Energy Frontier Research Center funded by the U.S. Department of Energy, Office of Science, Office of Basic Energy Sciences under Award Number DE-SC0001088.